Relating Structural and Functional Connectivity in MRI: A Simple Model for a Complex Brain

Arnaud Messé*, Habib Benali, and Guillaume Marrelec

***Abstract*—Advances in magnetic resonance imaging (MRI) allow to gain critical insight into the structure of neural networks and their functional dynamics. To relate structural connectivity [as quantified by diffusion-weighted imaging (DWI) tractography] and functional connectivity [as obtained from functional MRI (fMRI)], increasing emphasis has been put on computational models of brain activity. In the present study, we use structural equation modeling (SEM) with structural connectivity to predict functional connectivity. The resulting model takes the simple form of a spatial simultaneous autoregressive model (sSAR), whose parameters can be estimated in a Bayesian framework. On synthetic data, results showed very good accuracy and reliability of the inference process. On real data, we found that the sSAR performed significantly better than two other reference models as well as than structural connectivity alone, but that the Bayesian procedure did not bring significant improvement in fit compared to two simpler approaches. Nonetheless, we also found that the values of the region-specific parameters inferred using Bayesian inference differed significantly across resting-state networks. These results demonstrate 1) that a simple abstract model is able to perform better that more complex models based on more realistic assumptions, 2) that the parameters of the sSAR can be estimated and can potentially be used as biomarkers, but also 3) that the sSAR, while being the best-performing model, is at best still a very crude model of the relationship between structure and function in MRI.**

***Index Terms*—Bayesian inference, generative models, human brain connectivity, magnetic resonance imaging (MRI), simultaneous autoregressive model.**

I. Introduction

MAGNETIC resonance imaging (MRI) encompasses various imaging modalities that can be used to probe complementary information about the human brain. By tracking the movement of water molecules, diffusion-weighted imaging (DWI) provides relevant insight into the main pathways of white matter fibers connecting different brain regions [1], [2]. Functional MRI (fMRI), by contrast, measures metabolic and hemodynamic consequences of brain activity [3], [4]. Analysis of fMRI data, especially at rest, has been shown to successfully extract sets of brain regions that are functionally dependent and constitute brain networks [5], [6].

The functional dynamics of brain regions is reflective, at least in part, of the underlying anatomical connections [5]–[9]. Combining DWI and fMRI allows to investigate the relationship between structure and function within brain networks by relating coherent neuronal dynamics with the underlying structure of anatomical connectivity. In this perspective, a better understanding of the connection between structure and function relies on a better understanding of the relationship between DWI and fMRI data. Some recent results suggest that structure as extracted by DWI is tightly linked to function as extracted by fMRI (see [10] for a review). One way to link structure and function is to define a realistic generative model that, using biophysical neuronal functioning and anatomical wiring, is able to generate brain functional dynamics [11], [12]. However, such a framework is rather uneasy to explore due to the large number of parameters potentially involved and the complexity of any realistic forward model, leading to approaches that are bulky, computationally challenging and hard to evaluate. Besides, the precise selection of a given model and corresponding parameter values over other alternatives is an issue that remains unsolved, while potentially having dramatic influence on the simulations [12], [13].

In this paper, we present an original attempt to relate DWI and fMRI connectivity measures using structural equation modeling (SEM). SEM, also known as path analysis, has been a major way to examine effective connectivity in BOLD fMRI [14], [15]. SEM analysis requires the definition of the structure of interactions in the form of a directed graph. In a standard analysis, knowledge of the human brain anatomy and function is used to propose such a structure; the intensity of the existing connections are then estimated using fMRI data. By contrast, in the present approach, the structure of interaction is obtained (up to a global multiplicative constant) from DWI-based tractography. Such an approach leads to the definition of a spatial simultaneous autoregressive (sSAR) model [16], [17], see also [18] and [19] for applications in computational neuroscience and [20] for an application in MRI functional connectivity analysis. As mentioned above, realism comes at the expense of complexity: more complex models are usually harder to calibrate, in particular in terms of their model parameters. As a consequence, the gain in realism brought by a model could very well be offset by model parameters that are set to values that are far from optimal. By using a simple abstract model such as the sSAR, we set the balance between realism and estimability strongly in favor of estimability, hoping that the expected low

Manuscript received May 23, 2014; accepted July 16, 2014. Date of publication July 23, 2014; date of current version December 24, 2014. *Asterisk indicates corresponding author.*

*A. Messé is with the Laboratoire d'Imagerie Biomédicale, Sorbonne Universités, UPMC Univ Paris 06, INSERM, CNRS, UMCR 2, UMRS 1146, UMR 7371, F-75013 Paris, France, and also with the Department of Computational Neuroscience, University Medical Center Eppendorf, Hamburg University, 20246 Hamburg, Germany (e-mail: arnaud.messe@imed.jussieu.fr).

H. Benali and G. Guillaume are with the Laboratoire d'Imagerie Biomédicale, Sorbonne Universités, UPMC Univ Paris 06, UMR 7371, UMR_S 1146, F-75005 Paris, France.

Color versions of one or more of the figures in this paper are available online at http://ieeexplore.ieee.org.

Digital Object Identifier 10.1109/TMI.2014.2341732

performance obtained with such a simple model could be somewhat compensated by the improvement brought by the possibility to estimate the model parameters, and that the parameter values could be used as biomarkers. More precisely, our predictions were the following: i) A naive version of the sSAR with values from the literature performs worse that current widely accepted generative models; ii) adding a layer of parameter estimation improves the performance of the sSAR; iii) the more parameters are estimated, the better the fit; and iv) parameters estimated can be used to discriminate between well-known networks. To test these predictions, we compared the performances of functional connectivity simulated according to the sSAR model with parameters set according to three strategies (values from the literature, simple optimization of the coupling factor, and full Bayesian inference) with simulations from two reference models (rate model and neural mass model [21]) as well as structural connectivity alone. All analyses were performed at three different spatial scales, namely with parcellations of the brain into 160, 461, and 825 regions. Performance was quantified using both the predictive power (correlation between simulated and empirical data) and the mean square error. Results at all three scales and with the two measures agreed: prediction ii) and iv) were confirmed, while predictions i) and iii) turned out to be wrong. Regarding i), the sSAR performed better than the other models, regardless of how the model parameters were set. Regarding iii), the sSAR with full Bayesian inference scheme did not perform better than a simple optimization of the coupling parameter.

The outline of this article is the following. We first introduce the sSAR model and present some of its key features. We then present a Bayesian procedure to infer the parameter values and validate it on synthetic data. Finally, the model is applied to real MRI human brain data and compared to the reference models, showing the superiority of the sSAR model and the relative advantage of the Bayesian inference scheme. Consequences of these results are evoked in the discussion.

II. sSAR Model

A. From Structural Equations to Spatial Autoregression

In fMRI data analysis, predicting the pattern of functional interactions between brain regions from structural information is closely related to the concept of effective connectivity, which is defined as the effects that regions exert on one another [22]. In the following, we will turn our attention to structural equation modeling (SEM), which is a common model of effective connectivity in fMRI [14], [15]. More specifically, consider a network of R regions and denote by $y_r(t_n)$ the BOLD fMRI time course within region r $(1 \leq r \leq R)$ at time t_n $(1 \leq n \leq N)$. To account for nonzero mean of the fMRI data, we first decompose $y_r(t_n)$ into a baseline μ_r and a fluctuating signal $x_r(t_n)$

$$y_r(t_n) = \mu_r + x_r(t_n). \tag{1}$$

Assume now that the fluctuating signals are related through a model of structural equations, which relies on expressing each $x_r(t_n)$ as a linear function of other $x_s(t_n)$'s for $s \neq r$ [14], [15]

$$\boldsymbol{x}(n) = \boldsymbol{\Lambda x}(n) + \boldsymbol{e}(n)$$

where $\boldsymbol{x}(n) = [x_r(t_n)]_{r=1,\ldots,R}$ and $\boldsymbol{e}(n) = [e_r(t_n)]_{r=1,\ldots,R}$ are R-dimensional vectors. The model parameters $\boldsymbol{\Lambda} = (\Lambda_{rs})$ are known as the path coefficients; they specify the structure of spatial dependence between observations. $e_r(t_n)$ is some additive noise component that stands for the part of the noise that cannot be accounted for by the other variables. It is usually assumed to be normally distributed with zero mean and unknown variance σ_r^2, with a traditional assumption of spatial and temporal independence. In a standard SEM analysis, some Λ_{rs}'s are constrained to 0; the other coefficients, which are free to vary, must be estimated from data, usually by optimization of a cost function [23]. In the present study, we proceed differently. Instead of inferring the path coefficients from functional observations, we assume that each path coefficient Λ_{rs} can be expressed as $\Lambda_{rs} = \omega D_{rs}$, leading to a model

$$\boldsymbol{x}(n) = \omega \boldsymbol{D x}(n) + \boldsymbol{e}(n) \tag{2}$$

where $\boldsymbol{D} = (D_{rs})$ is an R-by-R matrix. This model is known as the simultaneous autoregressive (SAR) model [16], [24], [25]. In the present study, it is assumed that $\boldsymbol{D}$ is a matrix of structural connectivity obtained from DWI with the following properties: no self connections (i.e., $D_{rr} = 0$), and rows summing to 1 (i.e., $\boldsymbol{D}$ is right, or row, stochastic). With this last property, $\sum_{s \neq r} D_{rs} x_s(t_n)$ is a weighted average of the signals in regions $s \neq r$, with relative weights given by D_{rs}. ω is a real number in [0,1[coding for a global weight.[1] For each region r, the relative values of ω and σ_r^2 quantify the balance between the part of signal that can be accounted for by the activity of other regions and the structural properties of the network, $\sum_{s \neq r} D_{rs} x_s(t_n)$, and the part of the signal that is endogenous to region r, $e_r(t_n)$.

According to (1) and (2), $\boldsymbol{y}(n) = [y_r(t_n)]_{r=1,\ldots,R}$ is multivariate normal with mean $\boldsymbol{\mu}$ and covariance matrix

$$(\boldsymbol{I} - \omega \boldsymbol{D})^{-1} \boldsymbol{\Sigma} (\boldsymbol{I} - \omega \boldsymbol{D}^{\mathrm{t}})^{-1} \tag{3}$$

where $\boldsymbol{I}$ stands for the identity matrix, $\boldsymbol{\Sigma}$ is a diagonal matrix with $\mathrm{diag}(\boldsymbol{\Sigma}) = (\sigma_1^2, \ldots, \sigma_R^2)$, and "t" is the regular matrix transposition.

B. Inferring the Model Parameters

The sSAR model defined above has $2R+1$ parameters: $\boldsymbol{\mu}$ (R parameters), the diagonal elements of $\boldsymbol{\Sigma}$ (R parameters), and ω (1 parameter). In [18], ω was set to 0.5, while, it was set to 1 in [19]; in both cases uniform noise variance was assumed, $\sigma_r^2 = 1$ for all r. However, these settings were proposed for simulation purposes only. In our case, where we have to fit a model to data, we need to take the values for these parameters as unknown and estimate their probable values. We here propose to perform this step using Bayesian inference. In a Bayesian framework, all the information necessary for inference is contained in $\mathrm{p}(\boldsymbol{\mu}, \boldsymbol{\Sigma}, \omega | \boldsymbol{y})$, the posterior distribution of the model parameters, where, for the sake of simplicity, $\boldsymbol{y}$ stands for $(\boldsymbol{y}_n)_{n=1,\ldots,N}$. In the present study, we are mostly interested in the values taken by parameters ω and $\boldsymbol{\Sigma}$, $\boldsymbol{\mu}$ being a nuisance parameter. The distribution of interest is therefore $\mathrm{p}(\boldsymbol{\Sigma}, \omega | \boldsymbol{y})$. Given the model de-

[1] Note that, since the matrix $\boldsymbol{D}$ is row stochastic, its eigenvalues will be of module smaller than 1. As a consequence, $\boldsymbol{I} - \omega \boldsymbol{D}$ will have a nonzero determinant and be invertible for all $0 \leq \omega < 1$.

tailed in Section II-A, noninformative prior distributions and Bayes' updating rule, this distribution can be expressed as (see Appendix A for more details)

$$\mathrm{p}(\boldsymbol{\Sigma},\omega|\boldsymbol{y}) \propto |\boldsymbol{I}-\omega\boldsymbol{D}|^{N-1} \prod_{r=1}^{R} \left(\sigma_r^2\right)^{-\left[\frac{N-1}{2}+1\right]} \times e^{-\frac{1}{2}\sum_{r=1}^{R}\frac{f_r(\omega)}{\sigma_r^2}} \tag{4}$$

where $f_r(\omega)$ is the rth diagonal elements of

$$\boldsymbol{F}(\omega) = (\boldsymbol{I}-\omega\boldsymbol{D})\boldsymbol{S}(\boldsymbol{I}-\omega\boldsymbol{D}^{\mathrm{t}})$$

and where $\boldsymbol{m}$ and $\boldsymbol{S}$ are the usual sample mean vector

$$\boldsymbol{m} = \frac{1}{N}\sum_{n=1}^{N}\boldsymbol{y}_n$$

and sum of squares matrix

$$\boldsymbol{S} = \sum_{n=1}^{N}(\boldsymbol{y}_n-\boldsymbol{m})(\boldsymbol{y}_n-\boldsymbol{m})^{\mathrm{t}}.$$

From (4), one can compute the posterior distribution for ω, leading to (see Appendix A for more details)

$$\mathrm{p}(\omega|\boldsymbol{y}) \propto |\boldsymbol{I}-\omega\boldsymbol{D}|^{N-1} \prod_{r=1}^{R} f_r(\omega)^{-\frac{N-1}{2}}. \tag{5}$$

$\mathrm{p}(\omega|\boldsymbol{y})$ being 1-D, this distribution can be computed explicitly[2] on [0,1[. An estimator $\widehat{\omega}$ is given by the posterior expectation of ω, i.e.,

$$\widehat{\omega} = \int_0^1 \omega\mathrm{p}(\omega|\boldsymbol{y})\mathrm{d}\omega.$$

The posterior conditional distribution of $\boldsymbol{\Sigma}$ given ω is then given by

$$\mathrm{p}(\boldsymbol{\Sigma}|\boldsymbol{y},\omega) \propto \prod_{r=1}^{R} \left(\sigma_r^2\right)^{-\left[\frac{N-1}{2}+1\right]} e^{-\frac{N}{2}\sum_{r=1}^{R}\frac{f_r(\omega)}{\sigma_r^2}}. \tag{6}$$

This result shows that, given ω, each σ_r^2 has an inverse chi-square distribution with $N-1$ degrees of freedom and scale parameters $\sqrt{N f_r(\omega)/(N-1)}$. Since the expectation of such a distribution is $N f_r(\omega)/(N-3)$ [26, Appendix A], the posterior mean $\widehat{\sigma_r^2}$ can be readily computed as

$$\widehat{\sigma_r^2} = \frac{N}{N-3}\int f_r(\omega)\mathrm{p}(\omega|\boldsymbol{y})\mathrm{d}\omega.$$

This quantity can serve as an estimator for σ_r^2. Other statistics (such as the variance and highest probability density intervals) can be obtained by numerical sampling as follows. For $s = 1,\ldots,S$:

1) sample $\omega^{[s]}$ according to $\mathrm{p}(\omega|\boldsymbol{y})$ given by (5);
2) sample $\boldsymbol{\Sigma}^{[s]}$ according to $\mathrm{p}(\boldsymbol{\Sigma}|\boldsymbol{y},\omega^{[s]})$ given by (6).

[2]In practice, we took $\omega \in [0, 1-\epsilon]$ with $\epsilon = 10^{-3}$.

III. Validation on Synthetic Data

A. Data Generation

Validity of the inference procedure was assessed using synthetic data. In order to be close to real cases, we used structural connectivity matrices $\boldsymbol{D}$ obtained from the real datasets (see Section IV-B below). Then, we generated multivariate signals $\boldsymbol{y}$ with $\boldsymbol{\mu} = 0$ and a covariance matrix given by (3), with $\boldsymbol{\Sigma}$ diagonal. In order to assess the accuracy of the Bayesian procedure, we performed two experiments.

Experiment #1: We set $\omega = \omega_0$, with ω_0 ranging from 0.1 to 0.9 by increment of 0.1. For each ω, 5 000 samples were generated. For each sample, $\boldsymbol{D}$ was selected randomly among the 21 individual structural connectivity matrices and (σ_r^2) was generated randomly from the standard uniform distribution on [0,1].

Experiment #2: We set $\boldsymbol{\Sigma} = \boldsymbol{\Sigma}_0$, with $\sigma_r^2 = \sigma_0^2$ constant over regions and ranging from 0.1 to 0.9 by increment of 0.1. For each σ_0^2, 5 000 samples were generated. For each sample, $\boldsymbol{D}$ was selected randomly among the 21 individual structural connectivity matrices and ω was generated randomly from the standard uniform distribution on [0,1].

Both experiments were conducted for $N = 100$, 200 and 400 times points. The estimates $\widehat{\omega}$ and $(\widehat{\sigma_r^2})$ of the parameters were computed according to the Bayesian inference procedure (see Section II-B) and compared to the true values. The estimation error was quantified using the absolute difference between estimated and true values. For $\zeta \in \{\omega, \sigma_r^2\}$, the reliability of the inference procedure was assessed by monitoring the posterior probability of $[\hat{\zeta}-|\hat{\zeta}-\zeta_0|, \hat{\zeta}+|\hat{\zeta}-\zeta_0|[$, the smallest symmetric interval centered around the estimator $\hat{\zeta}$ that contains the true value ζ_0.

B. Results

The inference error and reliability for ω and σ^2 from Experiments 1 and 2 are shown in Fig. 1. The estimators $\widehat{\omega}$ and $\widehat{\sigma_r^2}$ were found to be very accurate regardless of sample size. As expected, the accuracy of $\widehat{\omega}$ increased with increasing ω_0 and N, while that of $\widehat{\sigma_r^2}$ decreased with increasing σ_0^2 and decreasing N. Inference reliability was confirmed, as $P(\hat{\zeta}-|\hat{\zeta}-\zeta_0| < \zeta < \mathrm{p}(\hat{\zeta}+|\hat{\zeta}-\zeta_0|)$ was very well approximated by the sampling histogram (similar results between ω and σ).

IV. Real Data

A. Data Acquisition and Preprocessing

Twenty one right-handed healthy volunteers were recruited within local community (11 males, mean age 22 ± 2.4 years). All participants gave written informed consent and the protocol was approved by the local ethics committee. Data were acquired using a 3T Siemens Trio TIM MRI scanner (CENIR, Paris, France). Functional resting-state MRI series were recorded using a single-shot, gradient-recalled echo-planar imaging sequence (repetition time (TR): 3290 ms; echo time (TE): 31 ms; 1.5 × 1.5 × 2.5 mm^3 voxels; 46 contiguous slices). Two hundreds fMRI volumes were acquired. The subjects were instructed to remain eyes closed and to reduce any mental effort. DWI data were recorded using a single-shot, echo planar imaging sequence (TR: 13 s; TE: 121 ms; 2 mm^3 isotropic

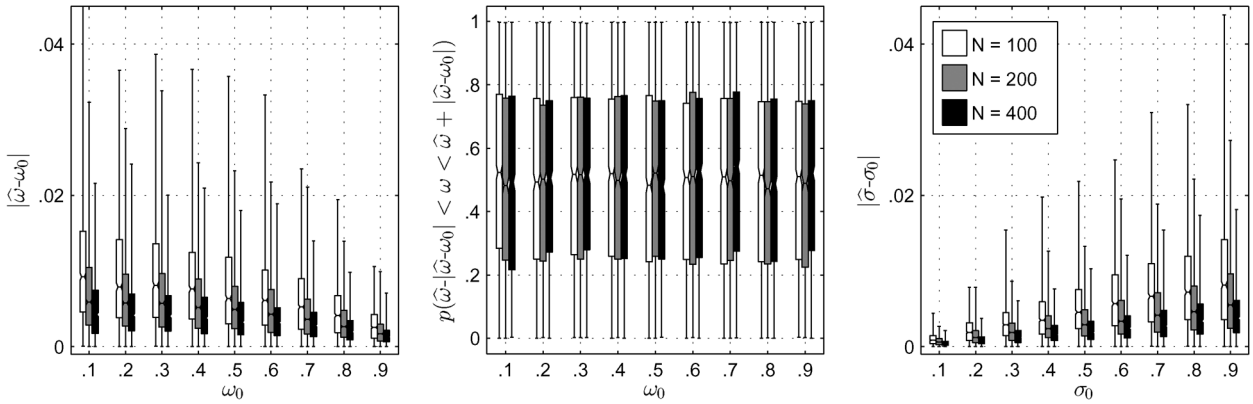

Fig. 1. Synthetic data. Parameters estimation for data sets of size $N \in \{100, 200, 400\}$. Are represented the absolute error (left) and reliability (middle) for ω in Experiment 1, as well as the absolute error for σ (right) in Experiment 2. For each box, the horizontal lines mark the quartiles and the whiskers extend to the most extreme data points.

voxels; 68 contiguous slices). Fifty encoding directions with $b = 1000\ \mathrm{s/mm^2}$ and a nonweighted image were acquired for each subject. A three dimensional, $\mathrm{T_1}$-weighted, magnetization prepared rapid gradient-echo volume was also acquired during the same scanning session (TR: 2.3 ms; TE: 2.98 ms; 1.1 $\mathrm{mm^3}$ isotropic voxels).

FMRI data were preprocessed using SPM5 software.[3] For each subject, the first four fMRI volumes were discarded to allow for T_1 equilibration, and the remaining 196 fMRI volumes were corrected for slice-timing and head motion, excessive motion (greater than 3 mm or 3°) was not present in any of the subjects' scans. The resulting data were then spatially smoothed using an isotropic 6 mm full-width-at-half-maximum Gaussian kernel. DWI images were corrected for eddy-current distortions using FSL, release 4.1[4] [27]. Spatial normalization using linear transformations (combination of three translations, three rotations, and one scale factor), between fMRI and DWI data and the anatomical volume, were computed for each subjects using FSL. Nonlinear spatial normalization was also computed from the T_1-weighted anatomical volume of each subject to the standard space of the Montreal Neurological Institute (MNI) for visualization purposes.

B. Extraction of Structural and Functional Features

The first step consisted of the definition of a set of regions of interest, in order to extract the intrinsic functional BOLD dynamic of each region and quantify the anatomical white matter fiber pathways between them.

Regions of Interest: The T_1-weighted anatomical volume of each subject was parcellated using Freesurfer software[5] [28] and the procedure described in [29]. The procedure divided the brain into cortical and subcortical gray matter and white matter. A labeled cortical surface from an average template brain was projected onto the individual cortical surfaces. For each subject, this provided a partition of the brain cortical surface and subcortical structures into 80 regions per hemisphere. Next, each cortical region of the average template brain was further subdivided into a set of small and compact regions of about 6 $\mathrm{cm^2}$ and 3 $\mathrm{cm^2}$, resulting in a parcellation of the whole cortex into 461 and 825 regions, respectively. These subdivisions were registered on the individual brains, and then projected into the fMRI and DWI subjects' native spaces using the linear transformations previously calculated.

Anatomical Wiring Connections: To quantify structural connectivity, a probabilistic white matter fiber tracking method [30] implemented in FSL was used to track all possible connections between all pairs of regions. For every voxel of the white matter we initiated 500 fiber samples, starting points were chosen randomly within the voxel space. The initial fiber orientation was randomly chosen, the fiber then growing in the two opposite directions; propagation step was set to 0.5 mm and maximal fiber curvature to 80° (no anisotropy constraint). Fiber tracking was stopped when a sample reached the cortical surface. An index of structural connectivity between two regions was then defined as the proportion of fiber samples connecting these two regions per unit surface. This index was further divided by the average fiber length to reduce bias towards longer fibers. This structural connectivity index allowed to build a $R \times R$ individual structural connectivity matrix $\boldsymbol{D}$ for each subject, D_{rs} being the structural connectivity index between regions r and s, with no self-connections (i.e., $D_{rr} = 0$). $\boldsymbol{D}$ was then thresholded at 0.001; supra-threshold values were kept as such.

BOLD Signal: The time series of all voxels within a given region were spatially averaged to form the representative signal of that region. To remove spurious sources of variance, linear and quadratic drifts, motion parameters, averaged ventricular, white matter and global brain signals were regressed out. Finally, the resulting time series were low-pass filtered ($<$0.1 Hz) [31], [32].

C. Simulating Functional Connectivity

For each subject, the inference procedure was applied to provide subject-specific estimates $\widehat{\omega}$ and $(\widehat{\sigma_r^2})$ that were reinjected into (3) to provide an estimator of functional connectivity. To assess the relative performance of the sSAR approach with Bayesian inference, we compared this approach (coined **sSARb**) to functional connectivity generated according to the following alternative strategies.

- **SC**: The matrix $\boldsymbol{D}$ of structural connectivity was directly used alone as a predictor of functional connectivity;

[3]Available online: www.fil.ion.ucl.ac.uk/spm/software/spm5/

[4]Available online: www.fmrib.ox.ac.uk/fsl/

[5]Available online: surfer.nmr.mgh.harvard.edu/

- **Rate** and **NM**: Two generative models: a linear model [21], [33] and a neural mass model [21], [34] (see Appendix B for more details). For each model, the connectivity parameter was obtained by optimization of either the predictive power (**Rate-pp** and **NM-pp**), that is, the Pearson correlation between simulated and empirical functional connectivity [21], [35], [36] or the mean square error (**Rate-mse** and **NM-mse**) at the coarse scale ($R = 160$) on the average subject, i.e., the subject that has an average matrix for both structural and functional connectivity;[6]
- **sSARn**: A 'naive' sSAR approach using *a priori* values for the sSAR parameters: $\omega = .5$ and $\sigma_r^2 = 1$ for all r, as in [18];
- **sSARo**: An 'optimized' sSAR approach with noise variance fixed $\sigma_r^2 = 1$ and where ω is selected in order to either maximize the predictive power (**sSARo-pp**) or minimize the mean square error (**sSARo-mse**) at the coarse scale on the average subject.

Performance was assessed using predictive power as well as the mean square error [35]. The various sSAR approaches were designed to provide information regarding the relative contributions of the sSAR model and the Bayesian inference: while sSARn and sSARo quantified the behavior of the sSAR model only, the difference in performance between sSARb and sSARo quantified the specific improvement brought by the Bayesian inference.

D. Results

1) Parameter Estimation: Results of sSAR parameter estimation from real data are summarized in Fig. 2 and Table I. Bayesian estimates of ω were relatively stable across subjects. All values were above the naive value of $\omega = 0.5$. While for $R = 160$ Bayesian estimates were around the values obtained by sSARo-pp and sSARo-mse, they were found to be under those values for $R = 461$ and $R = 825$. We also found that increasing R increased the estimates of ω of all sSAR models.

Estimates of the noise variance from sSARb varied significantly across subjects and regions for all spatial scales (two-way ANOVA; $p < 10^{-10}$). To test the spatial specificity of these estimates, we grouped regions according to the resting-state networks they belonged to. More specifically, we considered seven networks found in [37]: sensorimotor, auditory, executive control, frontoparietal, visual, default-mode, and subcortical. For each spatial scale, we kept the regions that overlapped at a level of at least 80% with a network. We found an effect of both subject and network on $\widehat{\sigma_r^2}$ for all scales (two-way ANOVA; $p < 10^{-10}$). The network effect is illustrated in Fig. 3.

2) Comparing Performances: Overall, all strategies had rather similar performance indices (Fig. 4). However, the differences between strategies were reproducible across subjects. Using permutation-based nonparametric paired testing (1000 permutations; threshold of 5% with Holm–Bonferroni correction for multiple comparisons [38]), we found significant differences across various model-pairs. Strategies could be ranked according to their performances across spatial scales and optimization schemes as follows (from best to worst):

- for an optimization based on the predictive power: sSARo-pp, sSARo-mse, sSARb, sSARn, Rate-pp, NM-pp, Rate-mse, SC, NM-mse;
- for an optimization based on the mean square error: sSARo-mse, sSARo-pp, Rate-mse, sSARb, sSARn, NM-mse, Rate-pp, SC, NM-ppsSARo-mse, sSARo-pp.

As expected, methods performed better when the coupling parameter was optimized using the measure also used to assess performance.

[6]The coarse-scale and average-subject approach was selected for computational reasons, as a finer-scale and/or subject-specific optimization would be intractable with the neural mass model in our case (one simulation takes around 14h for $R = 825$).

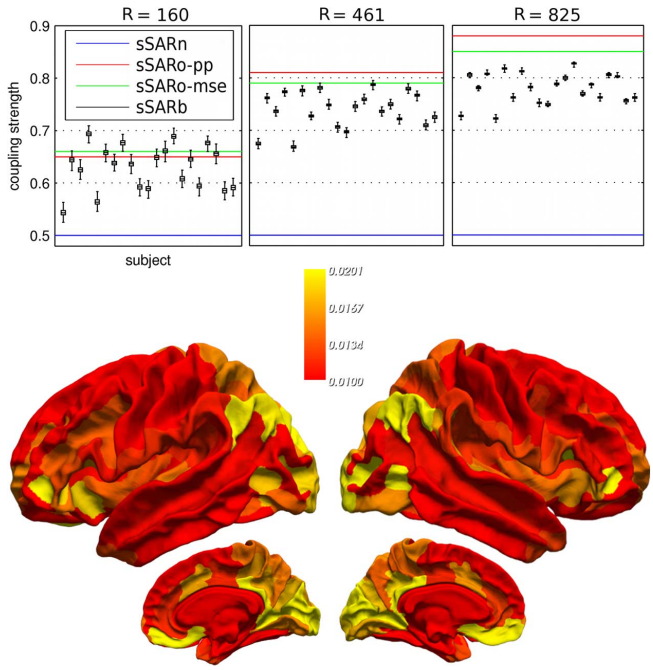

Fig. 2. Real data: sSAR parameter estimates. Top: Individual Bayesian mean $\pm$ standard deviation estimates of ω compared to the values used in sSARn ($\omega = 0.5$) and those obtained by sSARo-pp and sSARo-mse (see also Table I). Bottom: Illustration of the spatial distribution of $\widehat{\sigma_r^2}$ estimated with sSARb and averaged over subjects for the lowest spatial scale ($R = 160$).

TABLE I
Real Data: Estimates of ω. Values of $\widehat{\omega}$ Obtained by sSARo-pp and sSARo-mse

	$R = 160$	$R = 461$	$R = 825$
sSARo-pp	0.65	0.81	0.88
sSARo-mse	0.66	0.79	0.85

V. Discussion

In the present study, we used a spatial SAR model to relate structural and functional connectivity as measured in the human brain through DWI and fMRI, respectively. We tested the following predictions: i) a naive version of the sSAR with values from the literature performs worse that current widely accepted generative models; ii) adding a layer of parameter estimation improves the performance of the sSAR; iii) the more parameters are estimated, the better the fit; and iv) parameters estimated can be used to discriminate between well-known networks. While predictions ii) and iv) were confirmed, predictions i) and iii) turned out to be wrong. For i), the sSAR performed better than

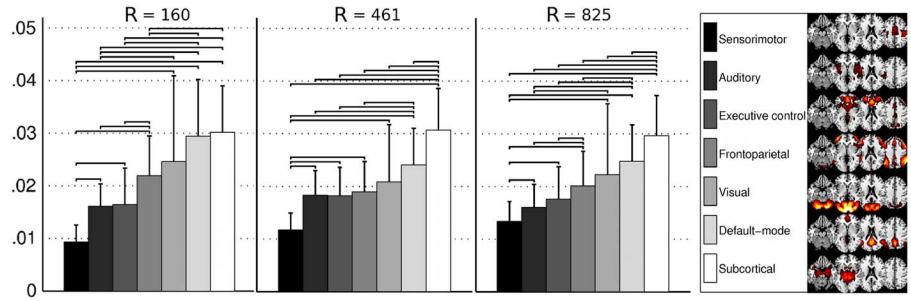

Fig. 3. Real data: Network-specific noise variance across subjects. For each network, subject and spatial scale, we computed the spatial average of $\widehat{\sigma_i^2}$ for all regions belonging to that network. Lines correspond to significant differences between networks (permutation test with 1000 permutations; threshold of 5% with Holm–Bonferroni correction).

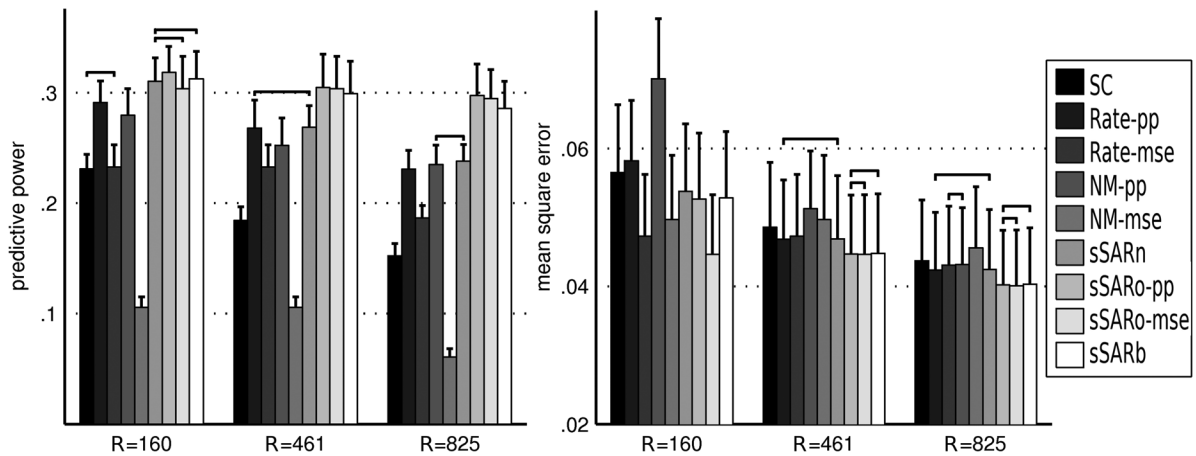

Fig. 4. Real data: Performance of simulation methods. Individual predictive power (left) and mean square error (right) of simulated functional connectivity from all strategies and scales. Each bar chart represents the mean and associated standard deviation over subjects. For the sake of clarity, lines correspond to *non*significant differences between networks (permutation test with 1000 permutations; threshold of 5% with Holm–Bonferroni correction).

the other models, regardless of how the model parameters were set and, regarding iii), the full Bayesian inference scheme that inferred all the model parameters did not perform better than the simple optimization of the coupling parameter.

A. The sSAR

Use of the sSAR as a generative model of functional connectivity has several advantages. As mentioned above, it predicts functional connectivity better than the two other models. As a consequence, it is, to our knowledge, the best tool to investigate the relationship between structure and function in MRI. Besides, this model is simple enough to allow inference. Using the Bayesian inference procedure, we saw that the noise variances so estimated differed from network to network. While the physiological meaning of the sSAR parameters remain to be clarified, it is our hope that, regardless of their meaning, these parameters could be useful biomarkers, may it be of certain networks or pathologies.

More conceptually, this study demonstrate that simple statistical models can be used to relate brain structure and function. Supported by the increase of computational power, more and more complex models of brain activity have been proposed and used in the MRI community to relate structural and functional connectivity [21], [35], [36]. These models rely on an increasingly detailed description of the biophysical and physiological processes underlying neuronal activity as well as its metabolic and hemodynamic consequences [10], [12], [39]. More recently, several attempts have been made to provide understanding of the structure-function relationship using more abstract and descriptive models, either with partial correlation and SEM [40], [41] or mixture models [42]–[44]. While realistic models rely on an analysis of the mechanisms underlying the generation of function from structure with parameters endowed with physiological interpretation, statistical models try to describe the data without any or much mechanistic interpretation. In this aspect, the sSAR model developed here has an ambiguous status. While it can be considered as mechanistic (at least at a macroscopic and abstract level, see Sections II-A and V-C), it also shares features with statistical models, such as a global description at the level of the data, the use of statistical distributions, and the possibility to infer parameter values. The fact that the sSAR models outperform more realistic models might be the sign that MRI can only be used to understand the relationship between brain structure and function at a statistical, not mechanistic, level. In any case, we hope that the present study, by making a link between realistic and more abstract approaches, will open the door to an even wider variety of modeling.

B. sSAR and Structural Information

DWI tractography provides information of undirected connectedness between regions, that is, it cannot differentiate between projections in one or in the other direction. By contrast,

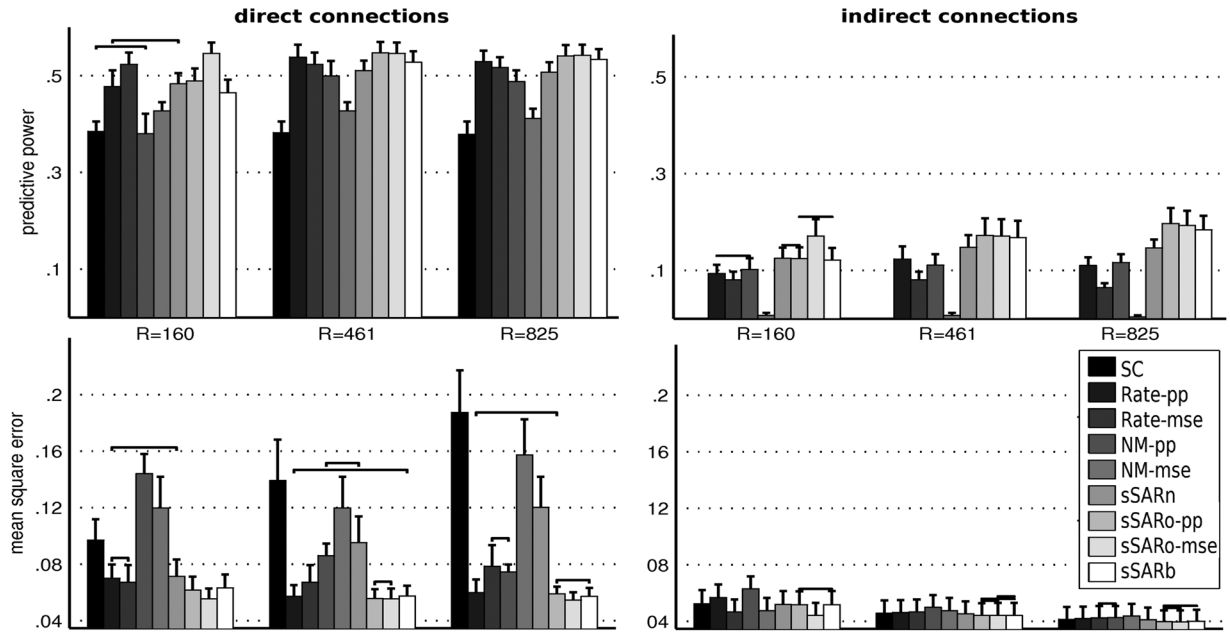

Fig. 5. Real data: Performance of simulation methods. Individual predictive power (top) and mean square error (bottom) of simulated functional connectivity from all strategies and scales for direct and indirect connections, left and right column, respectively. Each bar chart represents the mean and associated standard deviation over subjects. For the sake of clarity, lines correspond to *non*significant differences between networks (permutation test with 1000 permutations; threshold of 5% with Holm–Bonferroni correction).

SEM and its sSAR derivation were originally designed to handle directed graphs. This apparent contradiction of using information of undirected nature for a model that is intrinsically directed is not specific to the sSAR. Indeed, most generative models of brain activity, including the Rate and the Neural Mass models used in the present study, rely on directed information (e.g., the projections of neuronal entities onto one another) but use structural information from DWI (see, e.g., [21]). The way tractography is performed, it could result in a nonsymmetrical matrix, but this is rather considered as a spurious effect than a real indication of directionality between regions. As a consequence, the structural matrix is usually not the raw output from tractography but a post-processed version thereof. In our study, the postprocessing results in a matrix that is reciprocal (i.e., $D_{ij} \neq 0$ if and only if $D_{ji} \neq 0$) but not symmetrical (i.e., the weights of two reciprocal interactions may differ), see Sections II-A and IV-B. Even though the biological meaning of such matrices remains to be understood, they can be handled with no particular difficulty by all models tested here.

Another feature of DWI tractography is that it essentially provides information of monosynaptic connectivity. How this monosynaptic connectivity generates a pattern of functional connectivity that reflects both direct and indirect connectivity depends on the generative model selected. The advantage of the sSAR is that, because of its simplicity, the question can easily be answered in an analytical way. From (2), one has that

$$\boldsymbol{x}(n) = (\boldsymbol{I} - \omega \boldsymbol{D})^{-1} \boldsymbol{e}(n).$$

Using Taylor expansion for ω sufficiently small, one directly obtains that

$$\boldsymbol{x}(n) = \sum_{k=0}^{\infty} (\omega \boldsymbol{D})^k \boldsymbol{e}(n).$$

In other words, the sSAR can be interpreted as a process that propagates a node-specific signal $\boldsymbol{e}(n)$ to other nodes in one step [corresponding to $\omega \boldsymbol{D}\boldsymbol{e}(n)$], two steps [corresponding to $(\omega \boldsymbol{D})^2 \boldsymbol{e}(n)$], and so on. As a consequence, polysynaptic activity is modeled in the sSAR as a chain of monosynaptic connections. However, from a practical perspective, we observed that all models tested here performed worse for indirect connections than for direct connections at least in terms of predictive power (see Fig. 5). Whether this is an issue of the generative models themselves or rather of the tractography algorithm (which is likely to miss long range fibers such as homotopic connections) remains to be elucidated.

C. sSAR and Dynamics

The main feature of the present model is its simplicity. It does not try to first simulate neuronal activity and then model the BOLD signal as the metabolic and/or hemodynamic consequence of this activity; it is a direct model of the BOLD signal. Also, it is a model that is discrete and, as such, only attempts to explain the data and not the (necessarily continuous) underlying processes that lead to them. Even as a discrete model, it ignores temporal autocorrelation, since the data are assumed to be temporally independent. All in all, this model is merely an observational, or descriptive, model.

In this context, one could wonder in what measure the sSAR model and, more generally, SEM can be related to the underlying dynamics at the origin of the BOLD signal. One point is that SEM can be interpreted as describing the equilibrium point of the dynamic process [45]

$$\boldsymbol{z}(n+1) = \boldsymbol{\Lambda} \boldsymbol{z}(n) + \boldsymbol{b}(n+1). \tag{7}$$

While SEM has also been presented as the stationary version of this dynamic model [41], this fact has been challenged, since

stationarity implies equality of distributions at times n and $n+1$, not necessarily equality of the variables themselves [19]. In this context, how the sSAR could result from a dynamic process remains to be clarified. A possible explanation is that the sSAR model can emerge as the integration of a fast dynamic process at a slow time scale. More specifically, assume that the following continuous process:

$$\boldsymbol{z}(t+\delta t) = \boldsymbol{\Lambda}\boldsymbol{z}(t) + \boldsymbol{b}(t+\delta t)$$

occurs at a fast temporal scale. Then, integration of such a process between times t_n and $t_{n+1} = t_n + \Delta T$ with $\Delta T \gg \delta t$ yields

$$\int_{t_n}^{t_{n+1}} \boldsymbol{z}(t+\delta t)\mathrm{d}t = \boldsymbol{\Lambda} \int_{t_n}^{t_{n+1}} \boldsymbol{z}(t)\mathrm{d}t + \int_{t_n}^{t_{n+1}} \boldsymbol{b}(t+\delta t)\mathrm{d}t. \quad (8)$$

Setting

$$\boldsymbol{x}(n) = \int_{t_n}^{t_{n+1}} \boldsymbol{z}(t)\mathrm{d}t$$

and

$$\boldsymbol{e}(n) = \int_{t_n}^{t_{n+1}} \boldsymbol{b}(t)\mathrm{d}t.$$

Equation (8) can be expressed as

$$\boldsymbol{x}(n) = \boldsymbol{\Lambda}\boldsymbol{x}(n) + \boldsymbol{e}(n) + \boldsymbol{\varepsilon}(n)$$

with

$$\begin{aligned}\boldsymbol{\varepsilon}(n) = &\int_{t_{n+1}}^{t_{n+1}+\delta t} \boldsymbol{b}(t)\mathrm{d}t - \int_{t_n}^{t_n+\delta t} \boldsymbol{b}(t)\mathrm{d}t \\ &- \int_{t_{n+1}}^{t_{n+1}+\delta t} \boldsymbol{z}(t)\mathrm{d}t + \int_{t_n}^{t_n+\delta t} \boldsymbol{z}(t)\mathrm{d}t \\ &\approx [\boldsymbol{b}(t_{n+1}) - \boldsymbol{b}(t_n)]\,\delta t - [\boldsymbol{z}(t_{n+1}) - \boldsymbol{z}(t_n)]\,\delta t.\end{aligned}$$

$\boldsymbol{\varepsilon}(n)$ being of the order of δt, a small δt will lead to a small $\boldsymbol{\varepsilon}(n)$. In this case, it is legitimate to consider the sSAR as an approximation of the behavior of the process $\boldsymbol{x}(n)$.

D. Generative Models of Functional Connectivity

Regardless of its potential interpretation, we introduced the sSAR model in order to propose a simple mathematical model of BOLD fMRI covariations. Our rationale was that, since SEM has been successfully used in fMRI data analysis, a model that would be inspired from it might be a good candidate to account for fMRI intercorrelations. Most existing models are rather complex to understand and handle. With the sSAR, we were hoping to add to the modeler's toolbox a model that could give a crude sense of how brain structure and function are related. It turned out that all variants of the sSAR proposed here outperformed two current generative models of brain activity.

This result leads to quite interesting consequences. Depending on the perspective we take, it either emphasizes the good behavior of the sSAR compared to established models—a good behavior which remains to be explained with regard to its lack of physiological realism—or the inadequacy of the existing models to take functional connectivity into account. All in all, the maximum predictive power that was observed was 0.377, a quantity that leaves ample room for improvement. Note that better performances have been reported in the literature, but these were related to experiments on data selected to improve performance (e.g., direct connections [21], [35], intrahemispheric data [36] only, or matrix of structural connectivity with homologous connections added [20]). In these cases, we found that all models performed better than in the case with full data detailed in the present manuscript, but that the order of performance between models remained unaltered.

TABLE II
Real Data: Posterior Probabilities. $\log_{10}$ of the Posterior Probability of the Parameter Values Obtained With the Different Variants of the sSAR. Probabilities are Calculated Using Eq. (4) and Summarized as Mean (Standard Deviation) Across Subjects. All Values Should be Multiplied by 100

	$R = 160$		$R = 461$		$R = 825$	
sSARn	-13	(1)	-38	(4)	-77	(6)
sSARo-pp	-21	(1)	-98	(4)	-250	(5)
sSARo-mse	-22	(1)	-92	(3)	-227	(5)
SARb	524	(53)	1411	(131)	2500	(217)

E. Bayesian Inference

The fact that Bayesian inference did not bring a significant improvement to sSAR performance was evidenced for all three scales ($R = 160$, $R = 461$, and $R = 825$) and two measures of performance (predictive power and mean square error). This result came as a surprise. We do not think it could be attributed to a flaw in the inference process itself, which performed as expected on simulated data (see Section III). Under the assumptions made in Section II (including the generative model and the prior distributions), Bayesian analysis provides an assessment of the most probable values for the model parameters through the posterior probability distribution. This can be confirmed by calculating the posterior probability associated with the parameter values estimated with the other sSAR variants (sSAR-pp and sSAR-mse), which was found to be clearly smaller than when one takes the values estimated with sSARb (see Table II). The fact that these most probable parameters do not correspond to the ones that one would consider as best according to reasonable metrics might suggest that the model used is too crude. While the use of noninformative priors could be challenged, we do not believe that this choice matters that much, since we have a relatively large number of data compared to number of unknown parameters. By contrast, the use of a model as described in (1) and (2) might appear more problematic, in particular with respect to how the noise is taken into account. Indeed, the only "noise" considered here, i.e., $\boldsymbol{e}$ in (2), is noise in the statistical sense but it can still be interpreted in terms of the underlying SEM model. What would make sense would be to incorporate a quantity that takes measurement error in the model, e.g., by adding a noise term to (1). This new approach would in particular be compatible with sSAR-mse, since it will find the param-

eter values that minimize the mean square error of $\mu_r + x_r(t_n)$ compared to $y_r(t_n)$.

F. Perspectives

Future work includes testing alternative autoregressive models from the literature, such as autoregressive moving average, conditional autoregressive or hierarchical models [46]–[48], as well as a noisy version of the model of (1). One could also imagine different variants of the sSAR model, e.g., one with one coupling coefficient ω_r per region instead of a global ω. Of course, in the perspective of using the parameters from these models as biomarkers, it would be of great interest to derive Bayesian inference schemes for such models.

Moreover, in the context of simple models, it may be possible to have access to the model marginal likelihood, namely $\mathrm{p}(\mathrm{data}|\mathrm{model})$, either in closed form or numerically. This quantity is key to Bayesian model comparison. One could then perform hypothesis testing, for instance to test several competing indices of structural connectivity, strategies for fMRI time-series preprocessing (band filtering, regress out confound signals), or even resilience to anatomical lesions, and many others.

APPENDIX A
BAYESIAN INFERENCE

Let $\boldsymbol{\Sigma}$ be the diagonal matrix defined by $\mathrm{diag}(\boldsymbol{\Sigma}) = (\sigma_1, \ldots, \sigma_R^2)$. According to Bayes' updating rule, $\mathrm{p}(\boldsymbol{\mu}, \boldsymbol{\Sigma}, \omega|\boldsymbol{y})$ can be expressed as

$$\mathrm{p}(\boldsymbol{\mu}, \boldsymbol{\Sigma}, \omega|\boldsymbol{y}) \propto \mathrm{p}(\boldsymbol{\mu}, \boldsymbol{\Sigma}, \omega) \cdot \mathrm{p}(\boldsymbol{y}|\boldsymbol{\mu}, \boldsymbol{\Sigma}, \omega)$$

where "$\propto$" relates two expressions that are proportional. In this equation, $\mathrm{p}(\boldsymbol{\mu}, \boldsymbol{\Sigma}, \omega)$ stands for the prior distribution of the model parameters and $\mathrm{p}(\boldsymbol{y}|\boldsymbol{\mu}, \boldsymbol{\Sigma}, \omega)$ for the model likelihood. Both quantities can be expressed readily as follows.

A. Likelihood

According to the model described in Section II-A, the likelihood yields

$$\mathrm{p}(\boldsymbol{y}|\boldsymbol{\mu}, \boldsymbol{\Sigma}, \omega) \propto |\boldsymbol{I} - \omega\boldsymbol{D}|^N |\boldsymbol{\Sigma}|^{-\frac{N}{2}} e^{-\frac{1}{2}Q(\boldsymbol{\mu}, \boldsymbol{\Sigma}, \omega)}$$

where the quadratic term

$$Q(\boldsymbol{\mu}, \boldsymbol{\Sigma}, \omega) = \sum_{n=1}^{N} (\boldsymbol{y}_n - \boldsymbol{\mu})^{\mathrm{t}} (\boldsymbol{I} - \omega\boldsymbol{D})^{\mathrm{t}} \boldsymbol{\Sigma}^{-1} (\boldsymbol{I} - \omega\boldsymbol{D})(\boldsymbol{y}_n - \boldsymbol{\mu})$$

can be expanded as

$$\mathrm{tr}\left[F(\omega)\boldsymbol{\Sigma}^{-1}\right] + N(\boldsymbol{m} - \boldsymbol{\mu})^{\mathrm{t}} G(\boldsymbol{\Sigma}, \omega)(\boldsymbol{m} - \boldsymbol{\mu}).$$

In this expression, $\mathrm{tr}(\cdot)$ is the usual trace function, and $\boldsymbol{m}$ and $\boldsymbol{S}$ are the sample mean vector and sum of squares matrix as defined in the main text. $F(\omega)$ and $G(\boldsymbol{\Sigma}, \omega)$ are matrix functions of the sample and model covariance matrix, respectively

$$F(\omega) = (\boldsymbol{I} - \omega\boldsymbol{D})\boldsymbol{S}(\boldsymbol{I} - \omega\boldsymbol{D}^{\mathrm{t}})$$

and

$$G(\boldsymbol{\Sigma}, \omega) = (\boldsymbol{I} - \omega\boldsymbol{D}^{\mathrm{t}})\boldsymbol{\Sigma}^{-1}(\boldsymbol{I} - \omega\boldsymbol{D}).$$

Since $\boldsymbol{\Sigma}$ is assumed to be diagonal, we have

$$|\boldsymbol{\Sigma}|^{-\frac{N}{2}} = \prod_{r=1}^{R} \left(\sigma_r^2\right)^{-\frac{N}{2}}$$

and

$$\mathrm{tr}\left[F(\omega)\boldsymbol{\Sigma}^{-1}\right] = \sum_{r=1}^{R} \frac{f_r(\omega)}{\sigma_r^2}$$

where $f_r(\omega)$ is the rth diagonal element of $F(\omega)$. This leads to the following expression for the likelihood function:

$$\mathrm{p}(\boldsymbol{y}|\boldsymbol{\mu}, \boldsymbol{\Sigma}, \omega) \propto |\boldsymbol{I} - \omega\boldsymbol{D}|^N \prod_{r=1}^{R} \left(\sigma_r^2\right)^{-\frac{N}{2}} \times e^{-\frac{1}{2}\left[\sum_{r=1}^{R} \frac{f_r(\omega)}{\sigma_r^2} + N(\boldsymbol{\mu} - \boldsymbol{m})^{\mathrm{t}} G(\boldsymbol{\Sigma}, \omega)(\boldsymbol{\mu} - \boldsymbol{m})\right]}.$$

B. Prior Distributions

Not assuming any prior dependence between the model parameters, we can decompose $\mathrm{p}(\boldsymbol{\mu}, \boldsymbol{\Sigma}, \omega)$ as

$$\mathrm{p}(\boldsymbol{\mu}, \boldsymbol{\Sigma}, \omega) = \mathrm{p}(\boldsymbol{\mu})\mathrm{p}(\boldsymbol{\Sigma})\mathrm{p}(\omega).$$

Similarly, we assume no prior dependence between the elements of $\boldsymbol{\mu}$ or those of $\boldsymbol{\Sigma}$, leading to

$$\mathrm{p}(\boldsymbol{\mu}) = \prod_{r=1}^{R} \mathrm{p}(\mu_r)$$

and

$$\mathrm{p}(\boldsymbol{\Sigma}) = \prod_{r=1}^{R} \mathrm{p}\left(\sigma_r^2\right).$$

For each parameter, we assume a noninformative prior, yielding a uniform prior distribution for ω and each μ_r and a Jeffreys distribution for each σ_r^2, $r = 1, \ldots, R$, i.e.,

$$\begin{cases} \mathrm{p}(\omega) = 1 & \omega \in [0, 1[\\ \mathrm{p}(\mu_r) \propto \text{constant} & \mu_r \in]-\infty, +\infty[\\ \mathrm{p}\left(\sigma_r^2\right) \propto \left(\sigma_r^2\right)^{-1} & \sigma_r^2 > 0. \end{cases}$$

Note that the priors for μ_r and σ_r^2 are improper.

C. Joint Posterior Distribution

Bringing the prior distribution and the likelihood together yields for the joint posterior distribution

$$\mathrm{p}(\boldsymbol{\mu}, \boldsymbol{\Sigma}, \omega|\boldsymbol{y}) \propto |\boldsymbol{I} - \omega\boldsymbol{D}|^N \prod_{r=1}^{R} \left(\sigma_r^2\right)^{-\left[\frac{N}{2}+1\right]} \times e^{-\frac{1}{2}\left[\sum_{r=1}^{R} \frac{f_r(\omega)}{\sigma_r^2} + N(\boldsymbol{\mu} - \boldsymbol{m})^{\mathrm{t}} G(\boldsymbol{\Sigma}, \omega)(\boldsymbol{\mu} - \boldsymbol{m})\right]}.$$

D. Marginal Distributions

$\mathrm{p}(\boldsymbol{\mu}, \boldsymbol{\Sigma}, \omega|\boldsymbol{y})$, considered as a function of $\boldsymbol{\mu}$, is proportional to a multivariate normal distribution with mean $\boldsymbol{m}$ and covariance matrix $[NG(\boldsymbol{\Sigma}, \omega)]^{-1}$. Since

$$|G(\boldsymbol{\Sigma}, \omega)| = |\boldsymbol{I} - \omega \boldsymbol{D}|^2 \prod_{r=1}^{R} \sigma_r^2$$

integration with respect to $\boldsymbol{\mu}$ yields

$$\mathrm{p}(\boldsymbol{\Sigma}, \omega|\boldsymbol{y}) \propto |\boldsymbol{I} - \omega \boldsymbol{D}|^{N-1} \prod_{r=1}^{R} \left(\sigma_r^2\right)^{-\left[\frac{N-1}{2}+1\right]} \times e^{-\frac{1}{2}\sum_{r=1}^{R} \frac{f_r(\omega)}{\sigma_r^2}}. \tag{9}$$

As a function of $\boldsymbol{\Sigma}$, this distribution is proportional to a product of R inverse chi-square distributions with $N-1$ degrees of freedom and scale parameter $\sqrt{N f_r(\omega)/(N-1)}$. Integration with respect to $\boldsymbol{\Sigma}$ therefore leads to

$$\mathrm{p}(\omega|\boldsymbol{y}) \propto |\boldsymbol{I} - \omega \boldsymbol{D}|^{N-1} \prod_{r=1}^{R} f_r(\omega)^{-\frac{N-1}{2}}. \tag{10}$$

E. Estimation of the Parameters of Interest

$\mathrm{p}(\omega|\boldsymbol{y})$ being 1-D, this distribution can be computed explicitely on $[0, 1-\epsilon]$ with ϵ set to 0.001. An estimator $\widehat{\omega}$ is given by the posterior expectation of ω. Estimation of the noise variance parameters can then be performed as follows. The conditional posterior distribution of $\boldsymbol{\Sigma}$ given ω, $\mathrm{p}(\boldsymbol{\Sigma}|\boldsymbol{y}, \omega)$, is given by

$$\mathrm{p}(\boldsymbol{\Sigma}|\boldsymbol{y}, \omega) = \frac{\mathrm{p}(\boldsymbol{\Sigma}, \omega|\boldsymbol{y})}{\mathrm{p}(\omega|\boldsymbol{y})}$$

where $\mathrm{p}(\boldsymbol{\Sigma}, \omega|\boldsymbol{y})$ and $\mathrm{p}(\omega|\boldsymbol{y})$ are given by (9) and (5), respectively. Keeping only terms that depend on $\boldsymbol{\Sigma}$ yields

$$\mathrm{p}(\boldsymbol{\Sigma}|\boldsymbol{y}, \omega) \propto \prod_{r=1}^{R} \left(\sigma_r^2\right)^{-\left[\frac{N-1}{2}+1\right]} \cdot \exp\left[-\frac{N}{2}\sum_{r=1}^{R} \frac{f_r(\omega)}{\sigma_r^2}\right].$$

Appendix B
Alternative Generative Models

The **rate** model is a classical linear dynamic model of neuronal populations [49]

$$\tau \frac{\partial u_i(t)}{\partial t} = -u_i(t) + \omega \sum_{j \neq i} D_{ij} u_j(t) + \sigma \nu_i.$$

Here we have $\tau = 20$ ms; and $\sigma = 0.25$.

The **neural-mass** model is a nonlinear biophysical model of neuronal dynamics relying on the Hodgkin–Huxley model [50]. The main dynamical variables are the mean membrane potential of excitatory (V) and inhibitory populations (Z), which are governed by the conductance of ions channels (g). The total current flow across pyramidal cell membranes is given by

$$\begin{aligned}
\frac{\partial V_i}{\partial t} = &- m_{\mathrm{Ca}} \left[g_{\mathrm{Ca}} + r_{\mathrm{NMDA}} a_{ee} k \sum_j D_{ij} Q_{V_j}\right] (V_i - V_{\mathrm{Ca}}) \\
&- \left[g_{\mathrm{Na}} m_{\mathrm{Na}} + a_{ee} k \sum_j D_{ij} Q_{V_j}\right] (V_i - V_{\mathrm{Na}}) \\
&- g_{\mathrm{K}} W (V_i - V_{\mathrm{K}}) - g_{\mathrm{L}} (V_i - V_{\mathrm{L}}) \\
&+ a_{ie} Z Q_{Z_i} + a_{ne} I_\delta \\
\frac{\partial Z_i}{\partial t} = &\, b \left[a_{ii} V_i Q_{V_i} + a_{ni} I_\delta\right]
\end{aligned}$$

with $D_{ii} = (1-k)/k$, and where m_{ion} and V_{ion} are the fractions of open ion channels and the Nernst potential for that ion species, respectively. For large ion channels population, the fraction of open ion channels is given by the sigmoid-shaped neural activation function, except for the potassium channels that decay exponentially. Q_V and Q_Z represent the average firing-rates of excitatory and inhibitory neurons. $I_\delta$corresponds to nonspecific subcortical excitation; a_{xy} scales the x-to-y synaptic strength; and r_{NMDA} denotes the number of NMDA receptors relative to that of AMPA receptors. Parameters are set to values taken from [21].

Simulated fMRI BOLD signal was obtained from simulated neuronal activity by means of the Balloon–Windkessel hemodynamic model [51], [52]. Global mean signal was then regressed out from each region's time series. Finally, simulated FC was computed as Pearson correlation between simulated time series. After optimization, we generated three runs of 8 min BOLD activity and averaged the corresponding FCs to obtain the simulated FC for each dynamical model and each subject.

Acknowledgment

The authors are thankful to O. Sporns (Department of Psychology, Princeton University, Princeton, NJ, USA) and C. J. Honey (Department of Psychological and Brain Sciences, Indiana University, Bloomington, IN, USA) for providing the neural-mass model. The authors are grateful to Stéphane Lehéricy (Center for Neuroimaging Research, Paris, France) for providing us with the MRI data.

References

[1] S. Mori and J. Zhang, "Principles of diffusion tensor imaging and its applications to basic neuroscience research," *Neuron*, vol. 51, pp. 527–539, 2006.

[2] P. Hagmann, M. Kurant, X. Gigandet, P. Thiran, V. J. Weeden, R. Meuli, and J.-P. Thiran, "Mapping human whole-brain structural networks with diffusion MRI," *PLoS One*, vol. 2, p. e597, 2007.

[3] N. K. Logothetis, J. Pauls, M. Augath, T. Trinath, and A. Oeltermann, "Neurophysiological investigation of the basis of the fMRI signal," *Nature*, vol. 412, pp. 150–157, 2001.

[4] M. E. Raichle and M. A. Mintun, "Brain work and brain imaging," *Annu. Rev. Neurosci.*, vol. 29, pp. 449–476, 2006.

[5] J. S. S. Damoiseaux, S. A. R. B. Rombouts, F. Barkhof, P. Scheltens, C. J. J. Stam, S. M. M. Smith, and C. F. F. Beckmann, "Consistent resting-state networks across healthy subjects," *Proc. Nat. Acad. Sci. USA*, vol. 103, pp. 13 848–13 853, 2006.

[6] F. Esposito, T. Scarabino, A. Hyvarinen, J. Himberg, E. Formisano, S. Comani, G. Tedeschi, R. Goebel, E. Seifritz, and F. Di Salle, "Independent component analysis of fMRI group studies by self-organizing clustering," *Neuroimage*, vol. 25, pp. 193–205, 2005.

[7] J. L. Vincent, G. H. Patel, M. D. Fox, A. Z. Snyder, J. T. Baker, D. C. Van Essen, J. M. Zempel, L. H. Snyder, M. Corbetta, and M. E. Raichle, "Intrinsic functional architecture in the anaesthetized monkey brain," *Nature*, vol. 447, pp. 83–86, 2007.

[8] A. Cohen, D. Fair, N. Dosenbach, F. Miezin, D. Dierker, D. Vanessen, B. Schlaggar, and S. Petersen, "Defining functional areas in individual human brains using resting functional connectivity MRI," *Neuroimage*, vol. 41, pp. 45–57, 2008.

[9] E. Rykhlevskaia, G. Gratton, and M. Fabiani, "Combining structural and functional neuroimaging data for studying brain connectivity: A review," *Psychophysiology*, vol. 45, pp. 173–187, 2008.

[10] C. J. Honey, J.-P. Thivierge, and O. Sporns, "Can structure predict function in the human brain?," *Neuroimage*, vol. 52, pp. 766–776, 2010.

[11] B. Horwitz, "Simulating functional interactions in the brain: A model for examining correlations between regional cerebral metabolic rates," *Int. J. Bio-Medical Comput.*, vol. 26, pp. 149–170, 1990.

[12] M. Breakspear, V. Jirsa, and G. Deco, "Computational models of the brain: From structure to function," *Neuroimage*, vol. 52, pp. 727–730, 2010.

[13] M. Breakspear and V. Jirsa, "Neuronal dynamics and brain connectivity," in *Handbook of Brain Connectivity*, ser. Understanding complex systems, K. J. A. Scott, Ed. Berlin, Germany: Springer, 2007, pp. 3–64.

[14] A. R. McIntosh and F. Gonzalez-Lima, "Structural equation modeling and its application to network analysis of functional brain imaging," *Human Brain Mapp.*, vol. 2, pp. 2–22, 1994.

[15] F. Gonzales-Lima and A. R. McIntosh, "Analysis of neural interactions related to associative learning using structural equation modeling," *Math. Comput. Simulat.*, vol. 40, pp. 115–140, 1995.

[16] P. Whittle, "On stationary processes in the plane," *Biometrika*, vol. 41, pp. 434–449, 1954.

[17] K. Ord, "Estimation methods for models of spatial interaction," *Journal of the American Statistical Association*, vol. 70, pp. 120–126, 1975.

[18] G. Tononi, O. Sporns, and G. Edelman, "A measure for brain complexity: Relating functional segregation and integration in the nervous system," *Proc. Nat. Acad. Sci. USA*, vol. 91, pp. 5033–5037, 1994.

[19] L. Barnett, C. L. Buckley, and S. Bullock, "Neural complexity and structural connectivity," *Phys. Rev. E*, vol. 79, p. 051914, 2009.

[20] A. Messé, D. Rudrauf, H. Benali, and G. Marrelec, "Relating structure and function in the human brain: Relative contributions of anatomy, stationary dynamics, non-stationarities," *PLoS Computat. Biol.*, vol. 10, p. e1003530, 2014.

[21] C. J. Honey, O. Sporns, L. Cammoun, X. Gigandet, J.-P. Thiran, R. Meuli, and P. Hagmann, "Predicting human resting-state functional connectivity from structural connectivity," *Proc. Nat. Acad. Sci. USA*, vol. 106, pp. 2035–2040, 2009.

[22] K. J. Friston, C. D. Frith, and R. S. J. Frackowiak, "Time-dependent changes in effective connectivity measured with PET," *Human Brain Mapp.*, vol. 1, pp. 69–79, 1993.

[23] E. Bullmore, B. Horwitz, C. J. Honey, S. Brammer, M. ad Williams, and T. Sharma, "How good is good enough in path analysis of fMRI data?," *Neuroimage*, vol. 11, pp. 289–301, 2000.

[24] J. P. Lesage and P. Olivier, "Bayesian model averaging for spatial econometric models," *Geograph. Anal.*, vol. 39, pp. 241–267, 2007.

[25] V. de Oliveira and J. J. Song, "Bayesian analysis of simultaneous autoregressive models," *Sankhya: Indian J. Stat.*, vol. 70, pp. 323–350, 2008.

[26] A. Gelman, J. B. Carlin, H. S. Stern, and D. B. Rubin, *Bayesian Data Analysis*, ser. Stat. Sci., 2nd ed. Boca Raton, FL: Chapman Hall/CRC, 1998.

[27] S. M. Smith, M. Jenkinson, M. W. Woolrich, C. F. Beckmann, T. E. J. Behrens, H. Johansen-Berg, P. R. Bannister, M. De Luca, I. Drobnjak, D. E. Flitney, R. K. Niazy, J. Saunders, J. Vickers, Y. Zhang, N. De Stefano, J. M. Brady, and P. M. Matthews, "Advances in functional and structural MR image analysis and implementation as FSL," *Neuroimage*, vol. 23, pp. 208–219, 2004.

[28] B. Fischl, A. Van der Kouwe, C. Destrieux, E. Halgren, F. Segonne, D. H. Salat, E. Busa, L. J. Seidman, J. Goldstein, D. Kennedy, V. Caviness, N. Makris, B. Rosen, and A. M. Dale, "Automatically parcellating the human cerebral cortex," *Cerebral Cortex*, vol. 14, pp. 11–22, 2004.

[29] P. Hagmann, L. Cammoun, X. Gigandet, R. Meuli, C. Honey, V. Wedeen, and O. Sporns, "Mapping the structural core of human cerebral cortex," *PLoS Biol.*, vol. 6, p. e159, 2008.

[30] T. E. J. Behrens, H. Johansen-Berg, S. Jbabdi, M. F. S. Rushworth, and M. W. Woolrich, "Probabilistic diffusion tractography with multiple fibre orientations: What can we gain?," *Neuroimage*, vol. 34, pp. 144–155, 2007.

[31] M. Fox, D. Zhang, A. Snyder, and M. Raichle, "The global signal and observed anticorrelated resting state brain networks," *J. Neurophysiol.*, vol. 101, pp. 3270–3283, 2009.

[32] K. Van Dijk, T. Hedden, A. Venkataraman, K. Evans, S. Lazar, and R. Buckner, "Intrinsic functional connectivity as a tool for human connectomics: Theory, properties, optimization," *J. Neurophysiol.*, vol. 103, pp. 297–321, 2010.

[33] R. Galán, "On how network architecture determines the dominant patterns of spontaneous neural activity," *PLoS ONE*, vol. 3, p. e2148, 2008.

[34] C. Honey, R. Kotter, M. Breakspear, and O. Sporns, "Network structure of cerebral cortex shapes functional connectivity on multiple time scales," *Proc. Nat. Acad. Sci. USA*, vol. 104, pp. 10 240–10 245, 2007.

[35] J. Cabral, E. Hugues, O. Sporns, and G. Deco, "Role of local network oscillations in resting-state functional connectivity," *Neuroimage*, vol. 57, pp. 130–139, 2011.

[36] G. Deco and V. K. Jirsa, "Ongoing cortical activity at rest: Criticality, multistability, ghost attractors," *J. Neurosci.*, vol. 32, pp. 3366–3375, 2012.

[37] S. M. Smith and T. E. Nichols, "Threshold-free cluster enhancement: Addressing problems of smoothing, threshold dependence and localisation in cluster inference," *Neuroimage*, vol. 44, pp. 83–98, 2009.

[38] S. Holm, "A simple sequentially rejective multiple test procedure," *Scand. J. Stat.*, vol. 6, pp. 65–70, 1979.

[39] G. Deco, V. Jirsa, and A. McIntosh, "Emerging concepts for the dynamical organization of resting-state activity in the brain," *Nat. Rev. Neurosci.*, vol. 12, pp. 43–56, 2011.

[40] M. W. Woolrich and K. E. Stephan, "Biophysical network models and the human connectome," *Neuroimage*, vol. 80, pp. 330–338, 2013.

[41] F. Deligianni, G. Varoquaux, B. Thirion, D. J. Sharp, C. Ledig, R. Leech, and D. Rueckert, "A framework for inter-subject prediction of functional connectivity from structural networks," *IEEE Trans. Med. Imag.*, vol. 32, no. 12, pp. 2200–2214, Dec. 2013.

[42] A. Venkataraman, Y. Rathi, M. Kubicki, C.-F. Westin, and P. Golland, "Joint generative models for fMRI/DWI and its application to population studies," in *Proc. 13th Int. Conf. Med. Image Comput. Comput.-Assist. Intervent. (MICCAI'2010)*, 2010, pp. 191–199.

[43] A. Venkataraman, Y. Rathi, M. Kubicki, C.-F. Westin, and P. Golland, "Joint modeling of anatomical and functional connectivity for population studies," *IEEE Trans. Med. Imag,*, vol. 31, no. 2, pp. 164–182, Feb. 2012.

[44] M. Hinne, T. Heskes, C. F. Beckmann, and M. A. J. van Gerven, "Bayesian inference of structural brain networks," *Neuroimage*, vol. 66, pp. 543–552, 2013.

[45] J. Pearl, On the statistical interpretation of structural equations UCLA Cognitive Syst. Lab., 1995, Tech. Rep..

[46] T. Bailey and A. Gatrell, *Interactive Spatial Data Analysis*. London, U.K.: Longman Sci. Tech., 1995.

[47] S. Banerjee, B. P. Carlin, and A. E. Gelfand, *Hierarchical Modeling and Analysis for Spatial Data*, ser. Monographs Stat. Appl. Probabil. . London, U.K.: Chapman Hall/CRC, 2003.

[48] R. Haining, *Spatial Data Analysis. Theory and Practice*. Cambridge, U.K.: Cambridge Univ. Press, 2003.

[49] H. R. Wilson and J. D. Cowan, "Excitatory and inhibitory interactions in localised populations of model neurons," *Biophys. J.*, vol. 12, pp. 1–24, 1972.

[50] M. Breakspear, J. R. Terry, and K. J. Friston, "Modulation of excitatory synaptic coupling facilitates synchronization and complex dynamics in a biophysical model of neuronal dynamics," *Network: Computat. Neural Syst.*, vol. 14, pp. 703–732, 2003.

[51] R. Larter and S. Brent, "A coupled ordinary differential equation lattice model for the simulation of epileptic seizures," *Chaos*, vol. 9, pp. 795–804, 1999.

[52] K. J. Friston, "Dynamic causal modelling," *Neuroimage*, vol. 19, pp. 1273–1302, 2003.